https://doi.org/10.1016/j.jssc.2021.122478

The crystal structure of $Na_2CaAl_4O_8$ and its hydration behaviour

M. CANTALUPPI *
Earth Science Department "Ardito Desio", University of Milan, Via Botticelli 23, 20133, Milan, IT
marco.cantaluppi.it@gmail.com

F. CÁMARA
Earth Science Department "Ardito Desio", University of Milan, Via Botticelli 23, 20133, Milan, IT
fernando.camara@unimi.it

* Corresponding author

Abstract

$Na_2CaAl_4O_8$ represents a crystalline phase occurring in metal-slag and calcium aluminate cements. Despite the industrial implications of these materials, its crystal structure had not been yet solved. We have solved the crystal structure of $Na_2CaAl_4O_8$ by means of Single Crystal X-ray Diffraction from grains obtained from synthesis. From single Crystal analysis we demonstrate that $Na_2CaAl_4O_8$ is orthorhombic, with $P2_12_12_1$ space group, a = 7.2541(1), b = 10.4301(2), and c = 10.4348(2) Å and V = 1287.92 $Å^3$. The structure is characterized by a framework of corner-sharing aluminium centred tetrahedra, described as a stacking along [101] of (101) layers of composed of six-membered tetrahedral distorted rings; layers are linked by sharing some AlO_4 tetrahedra apices with Al tetrahedra forming the adjacent layers along [010], along with the Ca-centred octahedra. Na atoms occupy extra-framework spaces in two types of coordination, one being asymmetric, representing a hydrophilic point, explaining the water reactivity.

Keywords: Calcium Aluminate Cements, $Na_2CaAl_4O_8$, Calcium Aluminate phases, Structure Analysis.

1. Introduction

Calcium Aluminate Cements (CACs) represent an important type of cement with many significant advantages compared to Ordinary Portland Cement, such as rapid hardening, chemical (alkali-silica reaction and sulphate attack) and abrasion resistance. Consequently, they are mainly used in refractory and building chemistry applications [1,2,3,4,5]. CACs are usually classified according to their chemical composition: (*i*) standard CACs with low iron content (48-60% wt. Al_2O_3, < 3% wt. Fe_2O_3, 3-8% wt. SiO_2); (*ii*) standard CACs with high iron content (36-42% wt. Al_2O_3, 12-20% wt. Fe_2O_3, 4-8% wt. SiO_2); (*iii*) High Alumina Cements (HACs) (> 60% wt. Al_2O_3, < 1% wt. Fe_2O_3, < 0.5% wt. SiO_2) [1]. HACs represent the most important CACs for refractory castable and concrete with high early strength and sea water resistance [6]. HACs are usually obtained by heating a mixture of synthetic alumina and pure limestone at 1550 - 1600 °C [7]. However, hydrated lime ($Ca(OH)_2$), laterite, bauxite and different qualities of alumina (i.e. impure synthetic alumina) can also be used as alternative starting raw materials [1]. Currently, the use of alternative raw materials with a wide range of chemical composition and origins, such as laterite, iron-rich bauxite, low-grade alumina and blast furnace slags, appears the most challenging frontier in CACs manufacturing due to the limited supply of bauxite [8,9]. Nevertheless, these alternative raw materials always introduce minor and trace elements (i.e., manganese, titanium, copper, nickel, alkali elements, fluorine and chlorine) that could affect positively or adversely the cement manufacturing and the cement properties, as broadly investigated in Ordinary Portland Clinker (OPC) [10,11,12,13,14,15,16]. Notwithstanding, only a few studies have explored the effect of minor elements on CACs final properties, especially on iron, manganese and magnesium-rich raw materials [10,17,18,19]. Despite the evidence of a broad range of sodium content (0.1-1% wt. Na_2O) in synthetic alumina, which represents the most frequent minor elements in synthetic alumina, because of the Bayer process [20], just a few studies have been carried out to understand its effect, and only on simple systems and limited temperature range [21,22].

Brownmiller and Bogue [23] firstly studied the chemical system CaO-Al_2O_3-Na_2O (also called with cement nomenclature as C-A-N system) at high temperature, revealing the occurrence of an unknown sodium-bearing crystal phase $Na_4Ca_3Al_{10}O_{20}$ (reported as $N_2C_3A_5$), along with other known calcium aluminate crystal phases commonly occurring in HACs, such as $CaAl_2O_4$ (krotite, CA) and $CaAl_4O_7$ (grossite, CA_2). Ostrowski and Żelazny [24] and Verweij and Saris [25] studied in detail the alumina dominant system CaO-

Al_2O_3-Na_2O at temperature below 1250°C. From this they identified the occurrence of an unknown sodium-bearing crystal phase $Na_2CaAl_4O_8$ (reported as NCA_2), for which they proposed the potential for a tetragonal crystal structure from a powder diffraction pattern of a synthesis. This cannot be reconciled with the optical observations made by Brownmiller and Bogue [23] that reported biaxial interference figures. The occurrence of $Na_2CaAl_4O_8$ (NCA_2) was also reported to occur within metal slags [26]. Yu et al. [21,26] studied the crystallization of $Na_4Ca_3Al_{10}O_{20}$ ($N_2C_3A_5$) and the X-ray Powder Diffraction pattern without resolving its crystal structure, reporting an orthorhombic cell unit for $N_2C_3A_5$ with a tentative *P222* space group. Tian et al. [27] reported the formation of $N_2C_3A_5$ by adding up to a 4.26% mass fraction of Na_2O to $12CaO{\cdot}7Al_2O_3$ ($C_{12}A_7$) and referred to Ostrowski and Żelazny [24] for indexing of $N_2C_3A_5$ in their powder diffraction patterns – although the latter authors found $N_2C_3A_5$ when adding Na_2O to CA – but did not report any data on lattice parameters of $N_2C_3A_5$.

In this study we have attempted the synthesis and structure solution of one of these prominent NCA phases, NCA_2, and in doing so, highlighting that NCA_2 represents the same crystal phase $Na_4Ca_3Al_{10}O_{20}$ ($N_2C_3A_8$), firstly reported by Brownmiller and Bogue [23], followed by Sengo et al. [28] and Yu et al. [21,26] by comparing published X-ray data *vs* our synthesis one.

2. Sample preparation

$Na_2CaAl_4O_8$ was synthesised by mixing analytical certified grade reagents, such as aluminium acetate hexahydrate ($Al(OH)(C_2H_3O_2)_2$, >99.5% wt., Merck), sodium carbonate (Na_2CO_3, >99.3% wt., Merck) and calcium carbonate ($CaCO_3$, >99.6% wt. Merck), which were combined in 78.11% wt., 11.49% wt. and 10.40% wt., respectively, to result in the appropriate molar ratio (Table 1). A two-step approach was used in order to promote crystal growth: 1) pellets (10 x 5 mm) of the raw mix were prepared by using a double acting hydraulic press at 60 kN for 1 min, which were then heated at 1200±15° C for 24 h in a laboratory oven (Carbolite Model RWF 12/5 with SiC resistors) in a sealed Pt crucible; 2) powder of the raw mix was ground for 2 hours in a zirconia grinding media, increasing the reactivity by reducing the crystal size and increasing the amorphous content, and added in a Pt crucible with fragments of the previous heated pellets, then were heated with the same previous conditions. The selected composition is plotted in Fig. 1, (modified from the one obtained from the open-access PhaseDiagram-Web source of FactSage v. 7.3, which uses the

oxide database (FToxid) available at the Facility for the Analysis of Chemical Thermodynamics (FACT) at the Centre for Research in Computational Thermochemistry (CRCT) of the Ecole Polytechnique de Montreal and McGill University [29]). An isothermal section at 1200° C, obtained by Verweij and Saris from the numerous experimental data falling in the richer-Al_2O_3 portion (>50% wt. Al_2O_3) [25], is reported in Fig. 2: it is in good agreement with the same portion of the isothermal section obtained from the open-access PhaseDiagram-Web source of FactSage v. 7.3 reported in Fig. 1.

A portion of the run product was embedded in epoxy resin under-vacuum condition, due to the high porosity of the sample, and dry-out polishing conditions were applied using abrasive papers with decreasing grain size and finished with diamond paste (1 μm). An ultrasonic bath in hexane was carried out between every abrasive paper change to remove the residual powder derived from the previous polishing. Samples were finally covered with a sputtered graphite layer to ensure conductivity for microstructural and microchemical investigations.

Table 1. *Chemical composition of the raw meal expressed as weight and weight % oxides and mol. and weight % of used reagents.*

$Al(OH)(C_2H_3O_2)_2$ (g / % wt.)	**Na_2CO_3 (g / % wt.)**	**$CaCO_3$ (g / % wt.)**
2.2373 / 78.11	0.3292 / 11.49	0.2978 / 10.40
Al_2O_3 (mol / % wt.)	**Na_2O (mol / % wt.)**	**CaO (mol / % wt.)**
0.50 / 63.33	0.25 / 19.25	0.25 / 17.42

Fig. 1. *Isothermal section of ternary phase diagram for CaO-Al_2O_3-Na_2O (also called C-A-N using cement nomenclature [3]) at 1200 °C and ambient pressure obtained with FactSage software and accessible from FactSage 7.3 database [29]; the green circle represents the chemical composition of NCA_2, also the chemical composition of the experiment reported in Table 1; red circles represent crystal phases, whereas red lines represent crystal phases with solid solution, in the legend is reported the common cement nomenclature for crystal phases.*

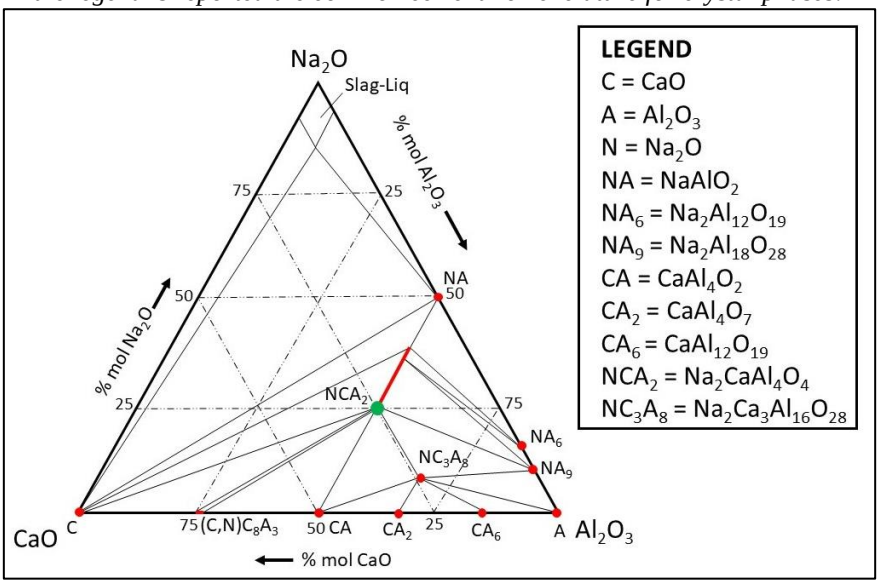

Fig.2. *Isothermal section of ternary phase diagram for CA-A-NA at 1200 °C at ambient pressure modified from Verweij and Saris [25]; the green circle represents the chemical composition of NCA_2, also the chemical composition of the synthesis; red circles represent crystal phases, whereas red lines represent crystal phases with solid solution; the nomenclature of crystal phases is the same of Fig. 1.*

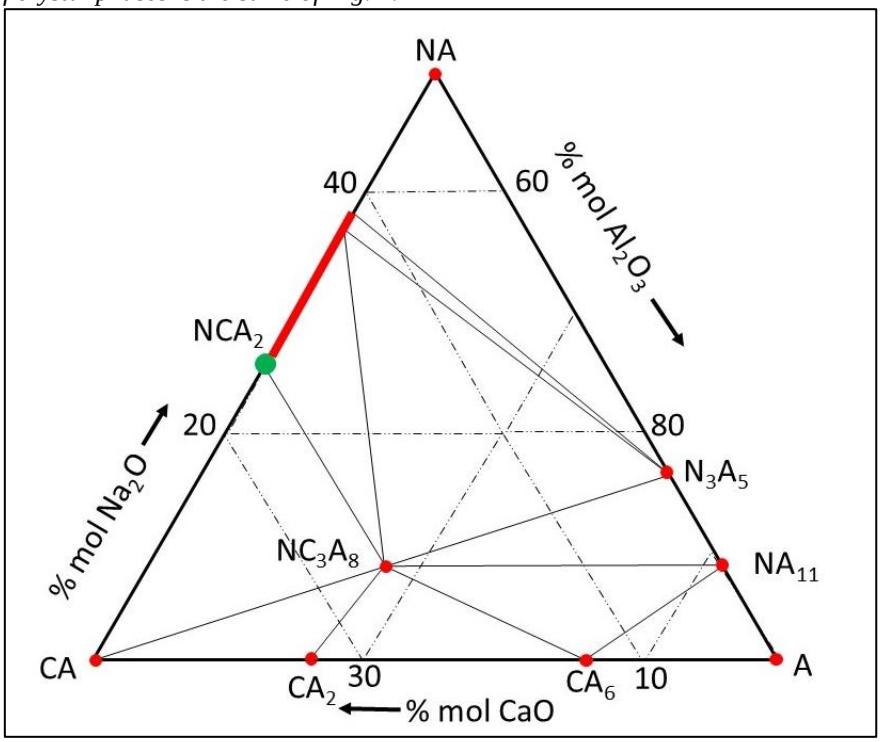

3. Analytical techniques

3.1. X-Ray Powder Diffraction (XRPD)

The anhydrous sample was ground and then pressed in a back-load sample holder. LXRPD data acquisition was carried out by a X'Pert PRO Diffractometer (PANalytical), in θ-2θ Bragg-Brentano geometry, equipped with an X'Celerator LPS detector. The 0.82-22.00 *d* (Å) range has been investigated using Cu*K*α radiation. All LXRPD analysis were performed with 40 kV current tension, 40 mA current intensity and 0.02° step size. The equivalent counting time was 100 s/step; each analysis was performed with fixed divergence slits angle at 0.25°.

3.2. Single crystal X-Ray Powder Diffraction (SCXRD)

The single-crystal X-ray study was done on a 77 × 93 × 143 μm crystal picked up from the synthesis run using a stereomicroscope. Diffraction data collection used a Rigaku Oxford Diffraction XtaLAB Synergy

diffractometer, equipped PhotonJet (Mo) X-ray Source operating at 50 kV and 1 mA, with a monochromatized Mo*K*α radiation and equipped with a HyPix hybrid photon counter (HPC) detector working at 62 mm from the crystal. A combination of 26 ω scans at different values of ϕ, χ e θ positions, with step scan 0.5° and exposure time 12 s per frame, was used to maximize redundancy and data coverage. We collected data up to 0.54 Å. Intensity data was extracted, scaled and corrected for absorption using CrysAlisPro 1.171.40.36a [30].

3.3. Scanning electron microscopy with energy dispersive analysis (SEM-WDS)

Quantitative chemical analyses were performed on resin embedded and polished samples using a JEOL JXA-8200 Electron MicroProbe Analyser in Wavelength-Dispersive mode, with an accelerating voltage of 15 kV, an electron probe spot size of 1μm, a beam current of 10 nA, a counting times of 30 s on peaks and 10 s on backgrounds. The following elements were measured: Si, Al, Ca, Fe, K, Mg and Na. Natural kyanite (Al_2SiO_5, for Al, Si, TAP Kα-lines), anorthite ($CaAl_2Si_2O_8$, for Ca. PET Kα-line), fayalite (Fe_2SiO_4, for Fe, LIF Kα-line), K-feldspar ($KAlSi_3O_8$, for K, PET Kα-line) and olivine ($(Mg,Fe)_2SiO_4$, for Mg, TAP Kα-line), omphacite ($(Na,Ca)(AlMg)Si_2O_6$, for Na TAP Kα-line) have been employed as standards. Raw data were corrected for matrix effects using a conventional ΦρZ routine in the JEOL soft-ware package.
Polished sections were also investigated by means of a Zeiss EVO MA15 Scanning Electron Microscope operating with an acceleration current of 15 kV, a beam size of 100 nm and a working distance of 11 mm, with an image resolution of 1024 x 730 pixels. Microstructural analysis was performed using detection of BackScattered Electrons (BSE).

4. Results

4.1 SEM and EMPA-WDS

The polished mount was covered by evaporated carbon layer and observed using Back Scattered Electrons (BSE). BSE and EMPA-WDS analysis highlighted microstructural features and chemical composition of phases, hereafter reported (Fig. 3, Table 2):

- a sodium-rich phase with an empirical formula of $Na_{1.9(1)}Ca_{1.1(1)}Al_{3.99(5)}Si_{0.01(1)}O_8$ (NCA_2), which represents the main phase; no clear idiomorphic shape of crystals was detected (Fig. 3a). SiO_2 and FeO contents occurred only as impurities coming from starting reagents;
- CA_2 occurred as minor phases, commonly forming dense clusters of 250 µm of diameter (Fig. 3b) with anhedral crystal shape with rounded edges and NCA_2 occurred as an interstitial phase (Fig. 3c).

Table 2. *EMPA-WDS results for CA_2 and NCA_2. n.d. not detected; standard deviation is reported in round brackets.*

Oxide (% wt.)	**NCA_2**	**CA_2**
K_2O	n.d.	n.d.
Na_2O	17.84(3)	0.15(3)
CaO	19.16(4)	21.38(4)
MgO	n.d.	n.d.
Al_2O_3	62.19(3)	78.35(7)
SiO_2	0.17(2)	0.04(4)
FeO	0.02(1)	0.03(1)
TiO_2	n.d.	n.d.
MnO	n.d.	n.d.
NiO_2	n.d.	n.d.
Total	99.38	99.95
Na	1.868	0.013
Ca	1.109	0.992
Al	3.959	3.998
Si	0.009	0.002
O	8	7

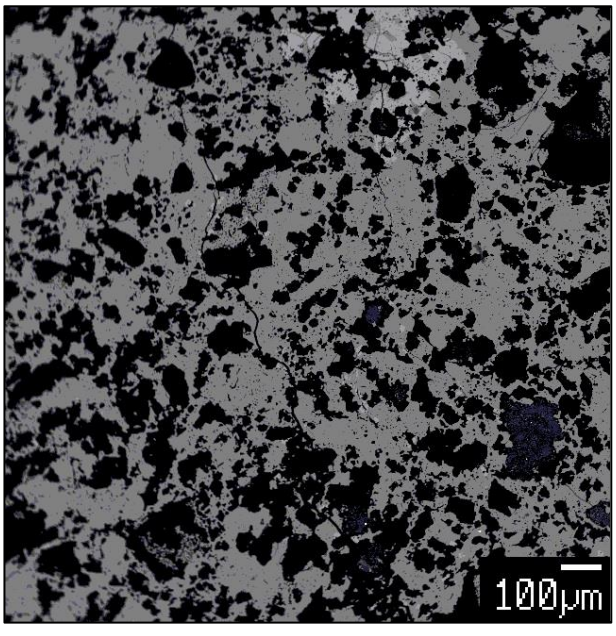

Fig. 3. *BSE images: a) an overview at lower magnification of the heated sample, highlighting the modal abundances of NCA_2 and CA_2; b) enlargement of the white dotted rectangle in the previous image, revealing a cluster of CA_2 crystals; c) enlargement at higher magnification of CA_2 cluster, highlighting the anhedral crystal shape and rounded edges for CA_2 crystals in contact with NCA_2.*

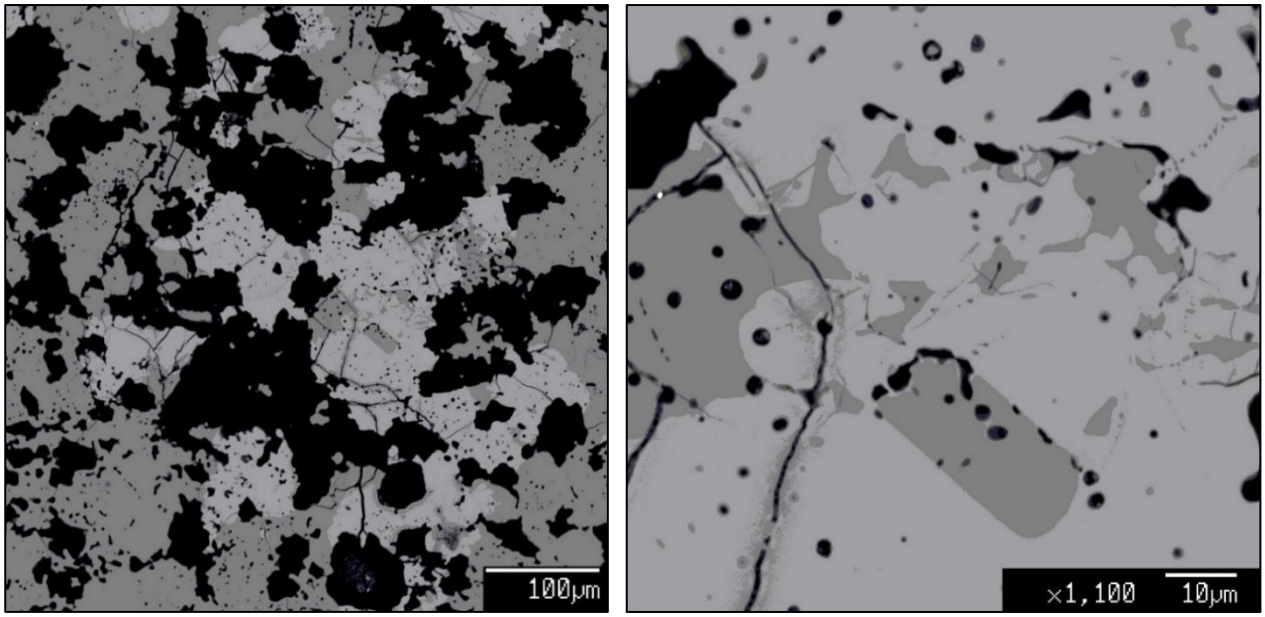

4.1 SCXRD and structure solution

Tested crystals showed merohedric twining and were be indexed in a first approach as tetragonal based on symmetric equivalents (R_{sym} = 11.4%). Analysis of systematic absences suggested a $P4_12_12$ space group. Yet it was not possible to solve the structure. Accurate analyses of intensity data led to a relaxation of the crystal symmetry to orthorhombic (although pseudo-tetragonal; see pseudo-precession in Fig. 3) and, based on best fit structure to data, the structure was solved in dual space mode starting with Patterson superimposition using SHELXT [31]. The best agreement factor ($R1$ = 0.165) in the non-centrosymmetric orthorhombic space group $P2_12_12_1$ among 56 tested, with an, obvious nonstoichiometric, Al_4CaNaO_9 chemistry proposed. Study of geometries of the solved model led to the exchange of one oxygen site by Na. Refinement of the model, using scattering curves for neutral atoms, and applying the twin law (011), and by allowing for anisotropic displacement parameters yielded a twin ratio of 0.463(2):0.537(2) and $R1$ value of 3.21% (see Table 3). Occupancy of Na at the Na sites was allowed to vary obtaining values of 0.99(1) and 0.97(1) showing a very slight deficiency of Na these sites. Moreover, Ca occupancy at the Ca site was firstly refined and resulted 0.994(3): this result suggested that Ca site should fully filled by Ca^{2+}, therefore, it was fixed to one and no Na^{+} was considered at the Ca site. The final stoichiometry obtained by structure refinement is $Na_{1.96}Ca[AlO_4]_4$, which requires some 0.01 apfu Si^{4+} for charge compensation in agreement with chemical

analyses reported in Table 2. The excess Ca reported in chemical analyses cannot be confirmed thus by structure refinement of the selected crystal. It is possible a certain degree of Na substitution by Ca and vacancies at the *Na*1 and *Na*2 sites. Structure refinement details are reported in Table 3, atom coordinates, site occupancy factors, equivalent isotropic displacement parameters and bond valence values [32] are reported in Table 4. Selected geometrical parameters are reported in Table 5. Anisotropic displacement parameters, refinement model and list of observed and calculated structure factors are included in the crystallographic information file, which is available as supplementary material.

Fig. 4. *Pseudo precession image of NCA_2 obtained using CrysAlisPro [29]. The image shows a reconstructed intensity on a hk0 section. Intensity distribution and geometry fits well with apparent tetragonal symmetry.*

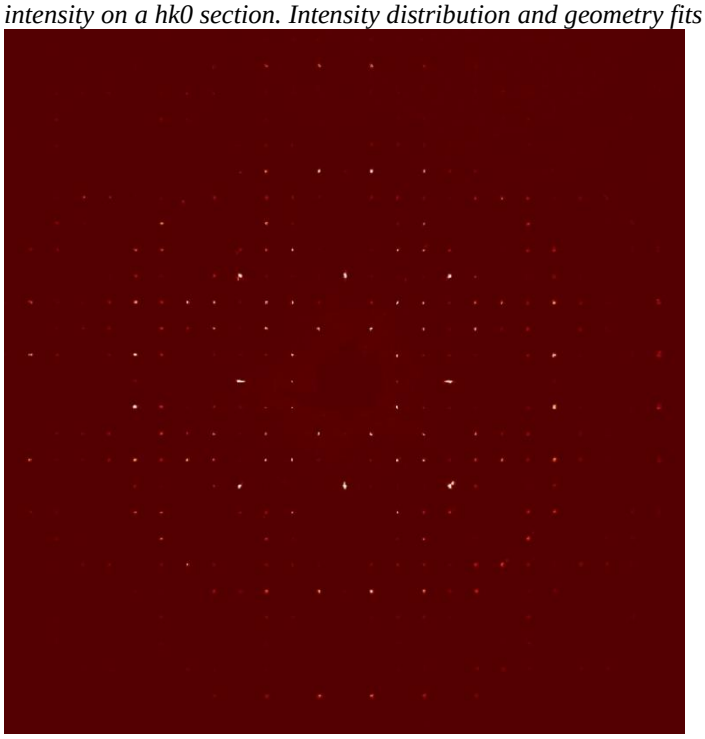

The observed structure is a three-dimensional framework of corner sharing (AlO_4) tetrahedra. Similar to tridymite topologies [33], the structure can be explained as the stacking of (101) layers built up by three types of distorted six membered rings of tetrahedra that line up along [010] (see Fig. 5a) building up 6^3 nets. The three types of rings have tetrahedra with vertices pointing up (U) or down (D) in the sequences UDUDUD (or 1-3-5) with trigonal appearance (A and B in Fig. 5), and with oblate appearance (C in Fig. 5). The rings are not planar with tetrahedra basis parallel to the (101) plane, and tetrahedra apexes points

alternatively have Up and Down orientation. Layers connect along [101] by sharing apical oxygen atoms and are shifted by (½ *a* –½ *c*).

There are four symmetrically independent Al-centred sites with a grand mean ≪Al–O≫ = 1.757(2) Å. The larger and most distorted one is *Al*3 (distortion index D.I. = 0.0082 D.I. following [34]) followed by *Al*1 (D.I. = 0.0077). Ca is in sixfold coordinated sites (*Ca* sites) and shares one edge with *Al*2 and one with *Al*3. Therefore, the octahedron is highly distorted (D.I. = 0.0196) and Ca is off-centred, showing three short and three longer Ca–O bond distances (Table 5). Na is present in two distorted sites with five-fold coordination (*Na*1and *Na*2). *Na*1 also shares an edge with the *Ca* site.

Considering the framework of AlO_4 tetrahedra, this develops channels along [001] that host chains of alkali centred polyhedra in the sequence *Ca*-*Na*1-*Na*2 (Fig. 6a,b).

In the synthesis minor CA_2 was also obtained. CA_2 can also be described as the stacking of six-membered rings of tetrahedra that line up along [001] (see Figure 5b), constituting 6^3 nets, although only one types of ring can be individuated, having tetrahedra with vertices pointing up (U) or down (D) in the sequences UUUDDD (or 1-2-3) with trigonal appearance. It can be also described as the merging of chains of AlO_4 groups sharing apices developing along [001]. Chains alternate their apex up and down along the [010] direction (Fig. 5b). Layers in CA_2 stack along [100] with a rotation of 180° and a shift of ½ *c*. between successive layers. In CA_2 channels along [001] that host CaO_7 polyhedra sharing and edge among them occur (Fig. 6c and d).

Fig. 5. *The 6^3 net of AlO_4 tetrahedra in NCA_2 (a) and CA_2 (b). The three types of 6R in NAC_2 are indicated with letters A, B and C. These have not tetrahedra basis parallel to the (101) plane, and tetrahedra apexes points alternatively have Up and Down orientation (marked with red dots in selected rings to better illustrate the concept). Red dashed arrow indicates the relative shift among layers stacked along [101. The 6^3 net of AlO_4 tetrahedra in CA_2 (b) shows only one type of 6R of type 1-2-3 (D). Figure obtained with Vesta 3.0 [35].*

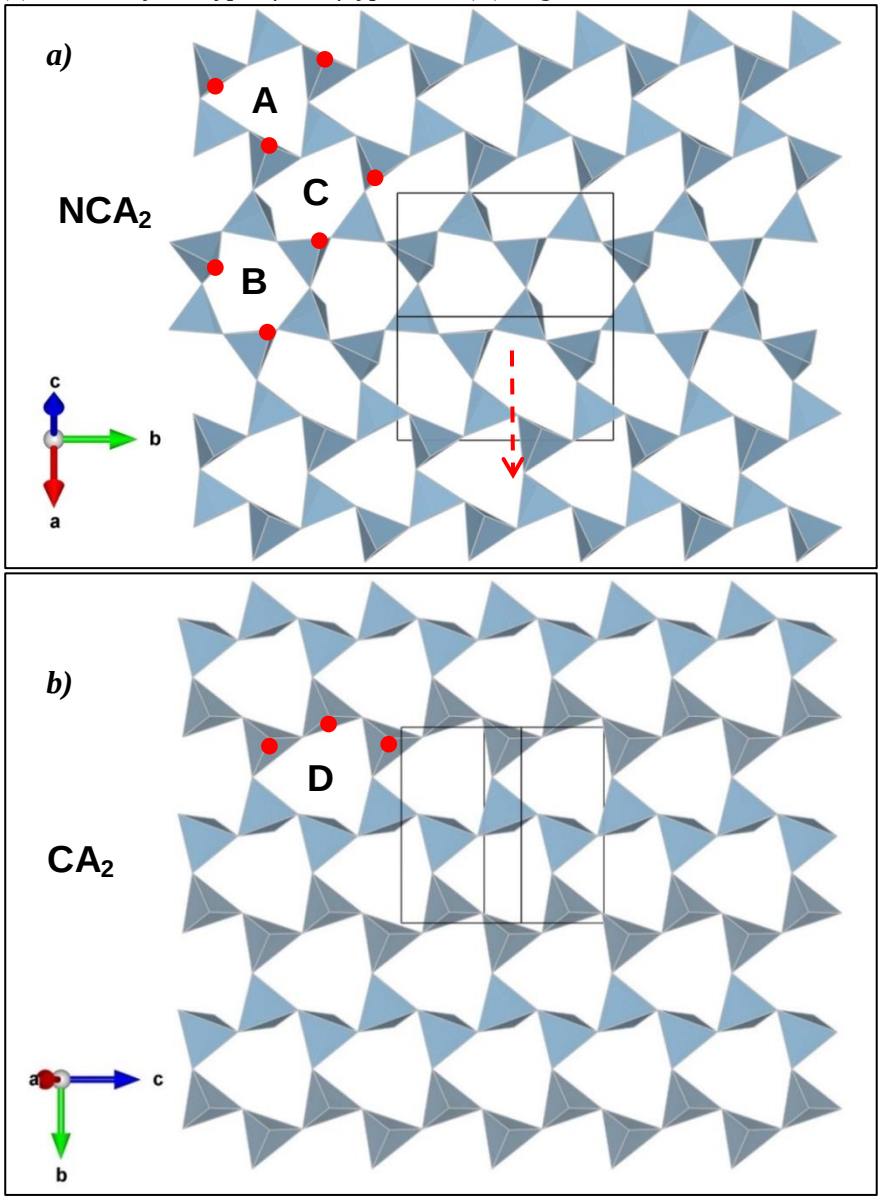

***Fig. 6**. Idealized scheme of channels along [001] represented by Al–Al distances in NCA_2 (a,b) and CA_2 (c,d). Ca (brown) and Na (yellow) sites are reported coordinating oxygen atoms to show their relative polyhedra. Thermal ellipsoids are plotted at the 90 % probability. Figure obtained with Vesta 3.0 [35].*

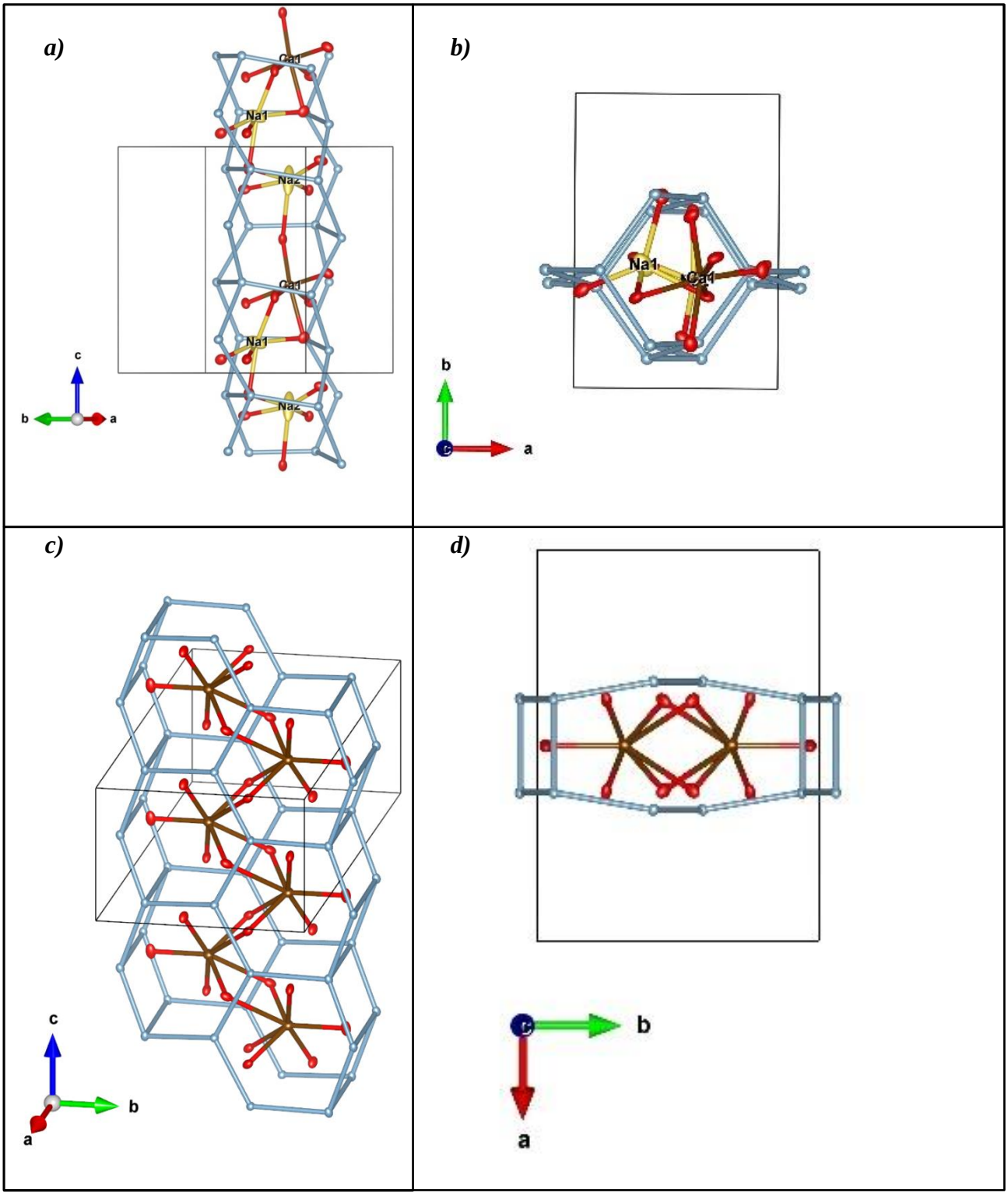

***Table 3**. Single-crystal X-ray diffraction data details for NCA_2.*

Crystal size (mm)	0.14 × 0.09 × 0.08
a (Å)	7.2541(1)
b (Å)	10.4301(2)
c (Å)	10.4348(2)
V (Å^3)	789.51(2)
Density (g/cm^3)	2.709
Range for data collection, θ (°)	3.4-40.3
Reciprocal space range *hkl*	$-13 \le h \le 13$ $-18 \le k \le 18$ $-18 \le l \le 19$
Set of measured reflections	55792
Unique reflections, R_{int} (%)	5049, 10.8
Absorption correction method	multi-scan SCALE3 ABSPACK
Refinement method	Full-matrix last-squares on F^2
Structural refinement program	SHELXL-2018
Number of refine parameters, restraints	139,0
wR^2 (%)	6.9
*R*1 (%) all data	3.75
*R*1 (%) for $I > 2\sigma(I)$	3.21
GooF	1.015
Weighting scheme	$w = 1/[\sigma^2(F_o^2) + (0.0311P)^2]$; where $P = (F_o^2 + 2F_c^2)/3$
Largest diff. peak and hole (±e$^-$/Å^3)	0.52 and –0.76

***Table 4**. Fractional atom coordinates and site occupancy, equivalent isotropic displacements and bond valence values (in valence units v.u.; calculated using Gagné and Hawthorne 2015 [32] values) for NCA_2.*

Atom		**s.o.f.**	***x/a***	***y/b***	***z/c***	U_{eq}	**b.v.**
Ca1	Ca	1	0.87909(11)	0.62686(5)	-0.11461(6)	0.00954(7)	1.812
Al1	Al	1	0.39344(12)	0.65750(8)	0.40101(8)	0.00747(13)	2.915
Al2	Al	1	0.62651(14)	0.64551(8)	0.15409(8)	0.00762(14)	2.920
Al3	Al	1	0.64027(12)	0.60031(8)	0.64849(9)	0.00758(13)	2.908
Al4	Al	1	0.12605(14)	0.39932(8)	0.40246(9)	0.00735(13)	2.937
Na1	Na	0.989(6)	0.3378(2)	0.41835(15)	0.13553(13)	0.0214(4)	0.756
Na2	Na	0.965(7)	0.4140(3)	0.86338(15)	0.6481(3)	0.0392(7)	0.838
O1	O	1	0.4635(3)	0.66896(19)	0.56079(19)	0.0120(3)	1.945
O2	O	1	0.8075(3)	0.55512(17)	0.09116(19)	0.0111(3)	1.867
O3	O	1	0.3048(3)	0.30725(18)	0.33558(19)	0.0105(3)	1.901
O4	O	1	0.3499(3)	0.81306(17)	0.34349(19)	0.0108(3)	1.815
O5	O	1	0.5719(3)	0.58587(18)	0.30767(19)	0.0110(3)	1.827
O6	O	1	0.5778(3)	0.59588(19)	0.81190(18)	0.0112(3)	1.956
O7	O	1	0.2005(3)	0.55827(18)	0.4054(2)	0.0128(4)	1.924
O8	O	1	0.4266(3)	0.65069(18)	0.05934(19)	0.0116(3)	1.851

271 **Table 5.** *Selected bond distances (Å) and angles (°) for NCA_2.*

*Al*1-O1	1.747(1)	*Al*2-O2	1.745(2)
*Al*1-O4	1.759(2)	*Al*2-O3	1.762(2)
*Al*1-O5	1.784(2)	*Al*2-O5	1.764(2)
*Al*1-O7	1.741(2)	*Al*2-O8	1.756(2)
<*Al*1-O>	1.758	<*Al*2-O>	1.757
V (Å^3)	2.77	V (Å^3)	2.77
D.I.	0.0077	*D.I.*	0.0037
*Al*3-O1	1.730(2)	*Al*4-O3	1.758(1)
*Al*3-O2	1.769(2)	*Al*4-O6	1.756(2)
*Al*3-O4	1.771(2)	*Al*4-O7	1.744(2)
*Al*3-O6	1.765(2)	*Al*4-O8	1.760(2)
<*Al*3-O>	1.759	<*Al*4-O>	1.754
V (Å^3)	2.77	V (Å^3)	2.76
D.I.	0.0081	*D.I.*	0.0030
*Ca*1-O2	2.332(2)	*Na*1-O1	2.493(2)
*Ca*1-O3	2.449(2)	*Na*1-O3	2.399(2)
*Ca*1-O4	2.478(1)	*Na*1-O4	2.527(3)
*Ca*1-O5	2.389(2)	*Na*1-O7	2.429(3)
*Ca*1-O6	2.338(2)	*Na*1-O8	2.631(2)
*Ca*1-O8	2.416(2)	<*Na*1-O>	2.496
<*Ca*1-O>	2.400	V (Å^3)	10.80
V (Å^3)	16.79	*D.I.*	0.0266
D.I.	0.0197		
		Ring B	
*Na*2-O1	2.252(3)	O4–O7–O6 (°)	135.91(10)
*Na*2-O2	2.925(3)	O6–O2–O3 (°)	111.59(9)
*Na*2-O5	2.579(3)	O3–O6–O4 (°)	127.53(10)
*Na*2-O6	2.461(2)	O6–O4–O7 (°)	100.28(9)
*Na*2-O7	2.302(3)	O7–O6–O2 (°)	100.00(9)
<*Na*2-O>	2.510	O2–O3–O6 (°)	93.93(9)
V(Å^3)	8.77		
D.I.	0.0818	Ring C	
		O8–O7–O4 (°)	158.53(10)
Ring A		O7–O4–O1 (°)	68.70(8)
O5–O6–O7 (°)	163.22(10)	O4–O1–O4 (°)	120.40(10)
O3–O7–O5 (°)	75.60(8)	O1–O4–O2 (°)	113.17(11)
O7–O5–O2 (°)	145.69(10)	O4–O2–O8 (°)	87.19(9)
O2–O4–O5 (°)	168.42(11)	O2–O8–O7 (°)	96.16(9)
O4–O5–O3 (°)	65.43(8)		
O5–O2–O4 (°)	70.75(8)		

272 Notes: *V* = polyhedral volume; D.I. = distortion index [34]
273

Fig. 7. *NCA_2 crystal structure highlighting hydrophilic position (hypothetical W reported in green) in the structure related to Na1,2 sites. The dashed lines show the shortest O…O distances (> 2.5 Å).*

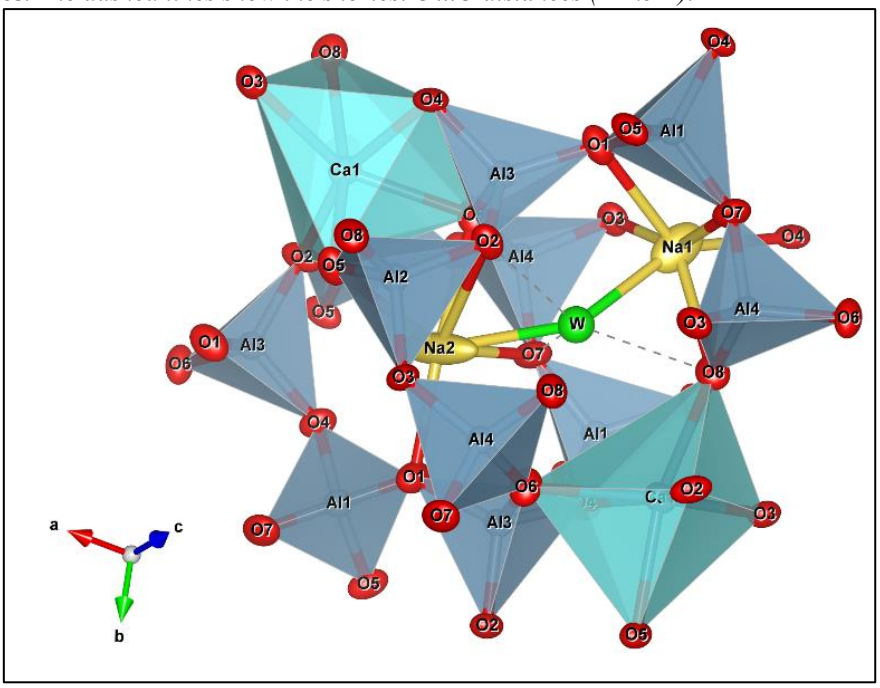

4.2. X-ray Powder Diffraction (LXRPD)

Rietveld Quantitative Phase Analysis (RQPA) was performed on the LXRPD pattern of synthesis run product by means of GSASII software [36,37], in order (*i*) to test the agreement with the crystal structure obtained from SCXRD analysis, (*ii*) to reveal changes in cell parameters due to ionic substitution between Na^+ and Ca^{2+} highlighted during EMPA-WDS analysis, and (*iii*) to detect and estimate the % wt. of crystal phases and comparing the mineral assemblage with phase diagram data (Fig. 1,2). The Rietveld refinement proceeded using with refining cell parameters, crystallite size, individual scale factor of crystal phases (NCA_2 and CA_2), zero shift and by using a Chebychev polynomial function with four terms to describe the background function. The instrumental broadening function implemented in GSAS II was obtained by refining the *U*, *V*, *W*, *X*, *Y* and *SH/L* parameters using a LaB_6 pattern collected with the same experimental set-up. The crystal structural model reported by Efremov et al. [38] for CA_2 was used. The reported crystal structure model was found using the open-access Crystal Open Database (COD) [39,40,41,42,43]. Bragg peaks positions of NCA_2 crystal structure from our study are in excellent agreement with those reported for NCA_2 by Verweij and Saris [25], and $N_2C_3A_5$ by Yu et al. [26], which suggest that all these correspond to the same phase. However, NCA_2 and $N_2C_3A_5$ may represent members of the same solid solution with changes in

the chemical composition among sodium and calcium: 2 Na^+ atoms could be replaced by Ca^{2+} and vacancies (2 $Na^+ \leftrightarrow Ca^{2+} + \square$), maintaining the charge balance. This would allow to go from NCA_2 to $N_2C_3A_5$, whereas Al_2O_3 is constant, i.e. no substitution at the (AlO_4) framework. Even if from a stoichiometric point of view this is a plausible substitution, the coordination at the *Na*1 and *Na*2 sites is not well suited for Ca, as observed by structure refinement of single crystal diffraction data. Moreover, bond-valence calculated values reported in Table 4 (0.756 and 0.838, respectively) are mostly incompatible with a divalent hosted at these sites. Alternatively, Na can substitute Ca at the *Ca* site. This is in fact what proposed by Verweij and Saris [25] and reported in Fig. 2 by the red line. This is more plausible looking at size, coordination and bond-valence incidence of the *Ca* site. It is noteworthy that our chemical analyses show Ca > 1 atom per formula unit and that the same result was found by Yu et al. [26]. Whereas the chemical analyses of Yu et al. [26] were made on unembedded grains with EDS, that may easily produce a low value for Na, our data have been obtained in polished surfaces and WDS analyses that should be much more accurate. At any rate, some Na decrease during microanalysis is plausible due to Na migration under the electron beam. The less biased datum is the model obtained from single crystal X-ray diffraction and structure refinement, and therefore we must suppose that the purported solid solution is due to analytical problems with chemical analyses.

Fig. 8. *LXRPD pattern, principal peaks for, NCA_2, NC_3A_8 and CA_2 are highlighted as black filled star, circle and diamond, respectively.*

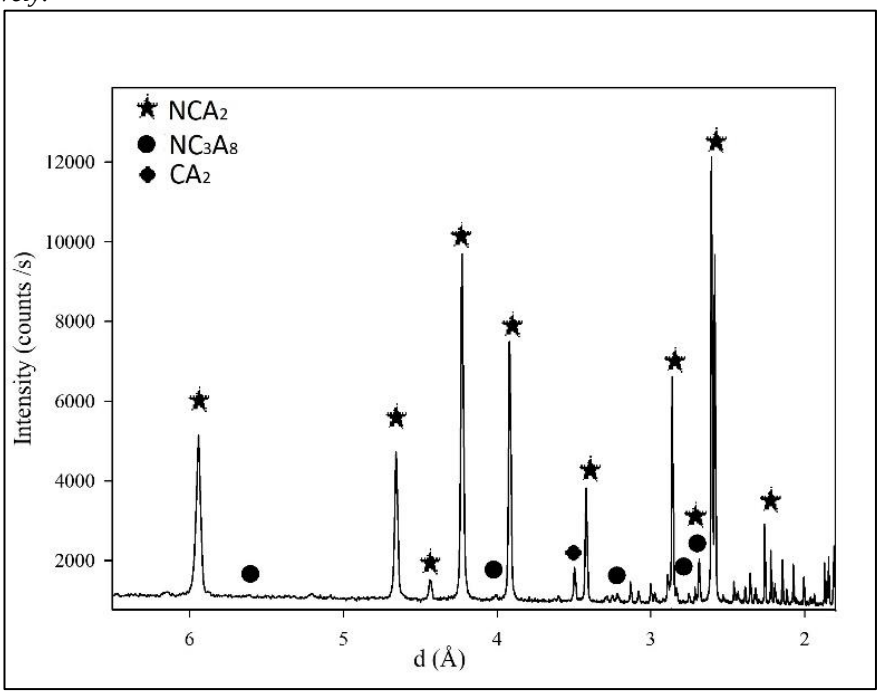

A detailed inspection of the pattern revealed the occurrence of minor amount of CA_2 (ICDD 33-1200) and Bragg peaks that fit with NC_3A_8, which may be indexed with a hexagonal cell ($a = b = 9.8436$ Å and $c = 6.9415$ Å) [25] but no crystal structure is still available. No NA ($NaAlO_2$, ICDD 33-1200) was detected despite many authors reported a partial decomposition of sodium-rich NCA_2 members producing NA and NCA_2 during cooling from high-temperature due to a solubility gap at lower temperature [23,25]. Table 6 reports the Rietveld Quantitative Phase Analysis (RQPA) for the synthesis run product, confirming that the sample is mainly composed of NCA_2 (>90% wt.) and minor amount of CA_2 (<2% wt.) and NC_3A_8. The estimation of NC_3A_8 % wt. was not possible due the lack of crystal structure, but it should be considered as a minor crystal phase (<2% wt.) due to the very low intensity of its Bragg peaks and the goodness of statistical parameters (R_{exp}, R_p, R_{wp} and GoF) (Fig. 9 and Table 6). Moreover, testing the crystal structure obtained by single crystal work on a powder pattern is important, because the most common quality control analysis on cement is XRD one.

Table 6. *Results from QXRPD; in the lower part are reported statistical values (R_p, R_{exp}, R_{wp}, GoF); e.s.d (1σ) in square brackets; Rietveld refinement was carried out without including NC_3Al_8, despite its evidence, because its crystal structure is still unknown.*

	NCA_2	**CA_2**
a (Å)	7.25088(6)	12.849(15)
b (Å)	10.4281(1)	8.887(2)
c (Å)	10.4393(1)	5.444(3)
β (°)	90	106.90(2)
V (Å^3)	789.345(9)	596.5(2)
% wt.	98.2(3)	1.78(9)
R_F (%)	7.06	11.48

R_{exp}	**R_p**	**R_{wp}**	**GoF**
4.50	8.05	11.94	2.65

Fig. 9. *RQPA pattern after refinement, CA_2 (Efremov et al.'s [38] crystal structure) and NCA_2 (crystal structure from our study) Bragg peaks are highlighted at the bottom as green and cyan vertical lines, respectively; moreover, NCA_2 Bragg peaks positions from Verweij and Saris [25], and Yu et al. [26] were reported as comparison as blue and red vertical lines, respectively; the observed and calculated patterns are reported as blue and green curve, respectively, whereas the background function is reported as a red line.*

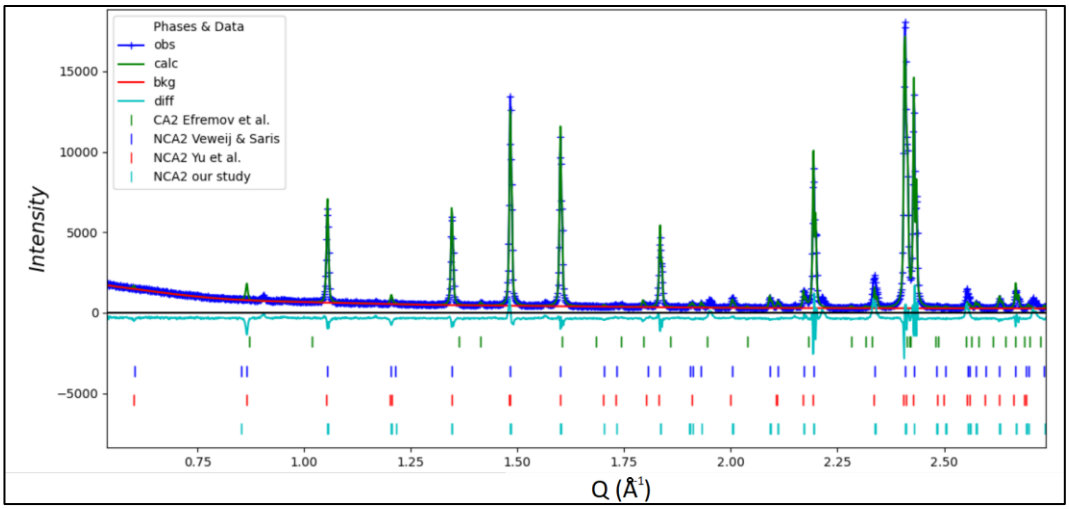

5. Discussion

NCA_2 was synthetised and its crystals studied by means of SCXRD, EMPA-WDS and SEM. The run product was studied by LXRPD analysis in order to testing the agreement between crystal structure obtained and other crystal phases synthetised during the experiment and observed by SEM. Cell parameters and space group were identified indicating a $P2_12_12_1$ space group with a = 7.2510 Å, b = 10.4304 Å and c = 10.4348 Å cell parameters. Yu et al. [26] reported that $N_2C_3A_5$ having $P222$ space group with a = 10.457 Å, b = 7.265 Å and c = 5.215 Å cell parameters; space group $P2_12_12_1$ of our model has higher symmetry than $P222$ and systematic absences for all (h00), (0k0) and (00l) diffraction Bragg peaks having odd integer numbers occur, which could explain the halving od c lattice parameter by Yu et al. [26], because the pseudotetragonal character lead to overlapping of suitable reflections to detect the doubling of the cell parameter. This is easily solved by looking at a 3D representation of the reciprocal space (see Fig. 4 for example). Verweij and Saris [25] reported N_2CA_2 as a tetragonal crystal structure with a = b = 10.4348 Å and c = 7.2539 Å cell parameters, and nevertheless the similarities on cell parameters with our data, this choice should be rejected because in clear contrast with optical properties found by Brownmiller and Bogue [23] that recognized biaxial positive crystals indicating orthorhombic or lower symmetry crystal system. The model we have obtained confirm therefore the optical behaviour and explain the pseudo symmetries that have leaded to propose tetragonal symmetry in previous studies. The occurrence of CA_2 and NC_3A_8 along with NCA_2 in the synthesis should be related only to very limited chemical composition shift from stoichiometric values of

364 $Na_2O{\cdot}CaO{\cdot}2Al_2O_3$ and/or to a limited loss in Na_2O, which could occur above 900 °C [23]. The phase
365 assemblage CA_2-NC_3A_8-NCA_2 should have reached the thermodynamic equilibrium considering the time left
366 at 1200 °C (24 hours), nonetheless our phase assemblage does not occur in the reported isothermal section at
367 1200 °C (Fig. 1,2) [25,29].
368 As reported in a previous work [44], the hydration of NCA_2 performed at 18 °C from 3 hours to 14 days
369 highlighted a pronounced reactivity with water: NCA_2 was completely reacted with water and started to
370 crystallise C_3AH_6 just after 1 day, whereas CA and CA_2 generally start to crystallise C_3AH_6 only during the
371 late hydration stage at ambient temperature (>28 days) [1]; after 14 days the phase assemblage is composed
372 of C_3AH_6, AH_3 and $NaAlO_2{\cdot}5/4H_2O$. The unusual coordination of Na in NCA_2, can explain the reactivity of
373 this phase during hydration (Fig. 7). In particular, the *Na*2 site that shows a 4+1 distorted coordination and
374 anisotropic displacement parameters elongated along [001] (Fig. 6a). Therefore, the occurrence of NCA_2 in
375 industrial HACs, which are mainly composed of CA and CA_2, during the hydration stage should enhance the
376 hydraulic reactivity and increase the conversion rate of metastable hydrates (CAH_{10} and C_2AH_8) to a more
377 stable mineral assemblage, such as hydrogarnet (C_3AH_6) and gibbsite (AH_3). Nevertheless, the increase of
378 the conversion from calcium aluminate hydrates to hydrogarnet could represent a problem for room
379 temperature application because it is generally associated to a strength reduction of paste due to the porosity
380 increase by the conversion reaction [1]; whereas for refractory application it could have a positive effect
381 because hydrogarnet is always formed during first thermal treatment, reducing shrinkage problem occurring
382 during heating [1]. Currel et al. [45] reported that substitution by sodium represents an acceleration additive
383 in HACs during hydration. Moreover, the occurrence of NCA_2 could be used to increase early strength also
384 for HACs rich in CA_2 and CA_6 which have extreme refractory properties but low reactivity with water [1].
385 On the whole, the development of NCA_2-rich HACs have the potential to enhance water reactivity and to
386 overcome problem related to the shortage of bauxite by using less pure Al-rich raw material, such as Al-rich
387 wastes [44].
388 The synthesis is composed of mainly NCA_2 with minor NC_3A_8 and CA_2 after 24 hours of heating at
389 1200±15 °C, but only NCA_2 and CA_2 were detected during SEM analysis: NC_3A_8 represents a minor crystal
390 phase with fine crystal size (as observed from diffraction by low intensity and rather broad peaks).
391 Moreover, microstructural features highlighted co-precipitation (coexistence) at high temperature of CA_2 and

NCA_2. The crystal phase NC_3A_8 was firstly observed by Verweij and Saris [25] at 1200 °C and does not appear on the liquidus surface, as reported Brownmiller and Bogue [23]: NC_3A_8 should decompose at higher temperature (>1200 °C). The mineral assemblage CA_2-NCA_2-NC_3A_8 does not appear in Verweij and Saris [25] isothermal section at 1200 °C (see Fig. 2) and the chemical composition of the sample falls within the CA-NCA_2-NCA_3 stability field: this difference in crystal phase assemblage should be related to a slightly higher heating temperature in our experiment with respect to bibliographical ones [25], leading the appearance of the NCA_2-CA_2 *tie-line* instead of CA-NC_3A_8 one and thus the formation of the CA_2-NCA_2-NCA_3 stability field, suggesting the reaction CA + NC_3A_8 → NCA_2 + CA_2.

6. Acknowledgements

We thank constructive reviews by three anonymous reviewers that helped to improve the text of the manuscript. Financial support by the grant Ricerca Locale 2014, Università di Milano and from the Italian Ministry of Education (MIUR) through the project "Dipartimenti di Eccellenza 2018–2022".

Reference

[1] H. Pöllmann, Calcium aluminate cements – Raw materials, differences, hydration and properties, RiMG 74 (2012) 1–82, https://doi.org/10.2138/rmg.2012.74.1

[2] P.C. Hewlett, Lea's Chemistry of Cement and Concrete, 2003. https://doi.org/10.1016/B978-0-7506-6256-7.X5007-3.

[3] H. F.W. Taylor, Cement chemistry, Thomas Telford Publishing, 1997

[4] W. Kurdowski, Cement and concrete chemistry, Springer, 2014

[5] M.C.G. Juenger, F. Winnefeld, J.L. Provis, J.H. Ideker, Advances in alternative cementitious binders, Cem. Concr. Res. 41 (2011). https://doi.org/10.1016/j.cemconres.2010.11.012.

[6] I.N. Chakraborty, A.K. Chattopadhyay, Manufacture of high alumina cement: An Indian experience, in Proceedings of the International Conference on Calcium Aluminate Cements (CAC) held at Heriot-Watt University Edinburgh, Scotland, UK, 16-19 July (2001) 25–33.

[7] R. Bolger, Non-refractory bauxite – Variety but not much spice, Industrial Minerals (1997) 21–29.

[8] M.F. Zawrah, N.M. Khalil, Utilisation of Egyptian industrial waste material in manufacture of refractory cement, Br. Ceram. Trans. 101 (2002) 225–228, https://doi.org/10.1179/096797802225004045

[9] S.A.S. El-Hemaly, N.M. Khalil, L.G. Girgis, Refractory castables based on barium aluminate cements, Br. Ceram. Trans. 103 (2003) 169–174, https://doi.org/10.1179/096797803225004954

[10] E.M.M. Ewais, N.M. Khalil, M.S. Amin, Y.M.Z. Ahmed, M.A. Barakat, Utilization of aluminum sludge and aluminum slag (dross) for the manufacture of calcium aluminate cement, Ceram. Int. 35 (2009) 3381–3388, https://doi.org/10.1016/j.ceramint.2009.06.008

[11] Á.G. De la Torre, A.J.M. Cuberos, G. Álvarez-Pinazo, A. Cuesta, M.A.G. Aranda, In situ powder diffraction study of belite sulfoaluminate clinkering, J. Synchrotron Rad. 18 (2011) 506–514, https://doi.org/10.1107/S0909049511005796

[12] K. Morsli, A.G. De la Torre, M. Zahir, M.A.G. Aranda, Mineralogical phase analysis of alkali and sulfate bearing belite rich laboratory clinker, Cem. Concr. Res. 37 (2007) 639–646, https://doi.org/10.1016/j.cemconres.2007.01.012

[13] J. Skibsted, T.F. Sevelsted, S.L. Poulsen, T.T. Tran, Studies on guest-ion incorporation in Portland cement — Part 1, ZKG Int. 66 (2013a) 66.

[14] J. Skibsted, T.F. Sevelsted, S.L. Poulsen, T.T. Tran, Studies on guest-ion incorporation in Portland cement — Part 2, ZKG Int. 66 (2013b) 46.

[15] J.I. Bhatty, Role of minor elements in cement manufacture and use, Portland Cement Association, (1995), https://trid.trb.org/view/461431

[16] H. Pöllmann, R. Obeste-Padtberg, Manganese in high alumina cement (HAC), in Proceedings of the International Conference on Calcium Aluminate Cements (CAC) held at Heriot-Watt University Edinburgh, Scotland, UK, 16-19 July (2001) 139–149.

[17] N.M. Khalil, S.AS. El-Hemaly, L. Girgis, Aluminous cements containing magnesium spinel from Egyptian dolomite. Ceram. Int. 27 (2001) 865–873, https://doi.org/10.1016/S0272-8842(01)00042-6

[18] E. Dourdounis, V. Stivanakis, G.N. Angelopoulos, E. Chaniotakis, E. Frogoudakis, D. Papanastasiou, D.C. Papamantellos, High-alumina cement production from FeNi-ERF slag, limestone and diasporic bauxite, Cem. Concr. Res. 34 (2004) 941–947, https://doi.org/10.1016/j.cemconres.2003.11.004

[19] M. Murat, F. Sorrentino, Effect of large additions of Cd, Pb, Cr, Zn, to cement raw meal on the composition and the properties of the clinker and the cement, Cem. Concr. Res. 26 (1996) 377–385, https://doi.org/10.1016/S0008-8846(96)85025-3

[20] A.R. Hind, S.K. Bhargava, S.C. Grocott, The surface chemistry of Bayer process solids: a review, Colloids Surf., A Physicochem. Eng. Asp. 146 (1999) 359–374, https://doi.org/10.1016/S0927-7757(98)00798-5

[21] H. Yu, X. Pan, B. Wang, W. Zhang, H. Sun, S. Bi, Effect of Na_2O on formation of calcium aluminates in $CaO–Al_2O_3–SiO_2$ system. T. Nonferr. Metal. Soc. 22 (2012) 3108–3112, https://doi.org/10.1016/S1003-6326(11)61578-1.

[22] J. Alex, L. Vandeperre, W.E. Lee, B. Touzo, C. Parr, Effect of Sodium on Microstructures and Thermoelastic properties of calcium aluminate cement–bonded refractories. J. Am. Ceram. Soc. 99 (2016) 1079–1085, https://doi.org/10.1111/jace.14046

[23] L.T. Brownmiller, R.H. Bogue, System $CaO-Na_2O-Al_2O_3$, J. Res. Natl. Bur. Stand. (U.S.) 8 (1932) 289–307.

[24] C. Ostrowski, J. Żelazny, Solid Solutions of Calcium Aluminates C_3A, $C_{12}A_7$ and CA with sodium oxide, J. Therm. Anal. Calorim. 75 (2004) 867–885, https://doi.org/10.1023/B:JTAN.0000027182.40442.fe

[25] H. Verweij, C.M.P.M Saris, Phase Formation in the System $Na_2O·Al_2O_3$-$CaO·A1_2O_3$-Al_2O_3 at 1200°C in Air, J. Am. Ceram. Soc. 69 (1986) 94–98 https://doi.org/10.1111/j.1151-2916.1986.tb04708.x

[26] H. Yu, X. Pan, Y. Tian, G. Tu, Mineral transition and formation mechanism of calcium aluminate compounds in $CaO-Al_2O_3-Na_2O$ system during high-temperature sintering, Int. J. Miner. Metall. Mater. 27 (2020) 924–932, https://doi.org/10.1007/s12613-019-1951-1.

[27] Y. Tian, X. Pan, H. Yu, G. Tu, Formation mechanism and crystal simulation of Na_2O-doped calcium aluminate compounds. Trans. Nonferrous Met. Soc. China, 26 (2016) 849−858, https://doi.org/10.1016/S1003-6326(16)64176-6

[28] S. Sengo, P. Romano Triguero, E. Zinngrebe, F. Mensonides, Tracing the origin of non-ferrous oxides in lamination defects on hot-rolled coils: mold slag entrainment vs submerged entry nozzle reaction Products, Metall. Mater. Trans. B48 (2017) 1690–1702, https://doi.org/10.1007/s11663-017-0928-6.

[29] C.W. Bale, E. Bélisle, P. Chartrand, S. Decterov, G. Eriksson, A. Gheribi, K. Hack, I.H. Jung, Y.B. Kang, J. Melançon, A.D. Pelton, S. Petersen, C. Robelin, J. Sangster, M-A. Van Ende, FactSage thermochemical software and databases, 2010–2016. Calphad 54 (2016) 35-53. https://doi.org/10.1016/S0364-5916(02)00035-4

[30] Agilent Technologies, CrysAlisPro Data Collection and Processing Software for Agilent X-ray Diffractometers, Technol. UK Ltd, Yarnton, Oxford, UK. (2014).

[31] G.M. Sheldrick, SHELXT - Integrated space-group and crystal-structure determination, Acta Crystallogr. Sect. A Found. Crystallogr. A71 (2015) 3–8, https://doi.org/10.1107/S2053273314026370.

[32] O.C. Gagné, F.C. Hawthorne, Comprehensive derivation of bond-valence parameters for ion pairs involving oxygen, Acta Crystallogr. B71 (2015) 562–578, https://doi.org/10.1107/S2052520615016297.

[33] J.V. Smith, Enumeration of 4-connected 3-dimensional nets and classification of framework silicates. I. Perpendicular linkage from simple hexagonal net, Am. Miner. 62 (1977) 703–709.

[34] W.H. Baur, The geometry of polyhedral distortions. Predictive relationships for the phosphate group. Acta Cryst. B30 (1974) 1195-1215, https://doi.org/10.1107/S0567740874004560

[35] K. Momma, F. Izumi, VESTA 3 for three-dimensional visualization of crystal, volumetric and morphology data, J. Appl. Crystallogr. 44 (2011) 1272–1276, https://doi.org/10.1107/S0021889811038970.

[36] B.H. Toby, R.B. Von Dreele, GSAS-II: the genesis of a modern open-source all purpose crystallography software package, J. Appl. Crystallogr. 46 (2007) 544–549, https://doi:10.1107/S0021889813003531.

[37] M.I. Aroyo, J.M. Perez-Mato, C. Capillas, E. Kroumova, S. Ivantchev, G. Madariaga, A. Kirov, H. Wondratschek, Bilbao Crystallographic Server: I. Databases and crystallographic computing programs, in: Zeitschrift Fur Krist. 221 (2006) 15–27, https://doi.org/10.1524/zkri.2006.221.1.15.

[38] Efremov V A, Gutnikov S I, Kartashov A A and Lazoryak. Average Grossite Crystal Structure. Personal Communication to COD (2012) http://www.crystallography.net/cod/3500014.html.

[39] R.T. Downs, M. Hall-Wallace, The American Mineralogist crystal structure database, Am. Mineral. 88 (2003) 247–250.

[40] S. Graulis, D. Chateigner, R.T. Downs, A.F.T. Yokochi, M. Quirós, L. Lutterotti, E. Manakova, J. Butkus, P. Moeck, A. Le Bail, Crystallography Open Database - An open-access collection of crystal structures, J. Appl. Crystallogr. 42 (2009) 726–729, https://doi.org/10.1107/S0021889809016690.

[41] S. Gražulis, A. Daškevič, A. Merkys, D. Chateigner, L. Lutterotti, M. Quirós, N.R. Serebryanaya, P. Moeck, R.T. Downs, A. Le Bail, Crystallography Open Database (COD): An open-access collection of crystal structures and platform for world-wide collaboration, Nucleic Acids Res. 40 (2012) D420–D427, https://doi.org/10.1093/nar/gkr900.

[42] S. Gražulis, A. Merkys, A. Vaitkus, M. Okulič-Kazarinas, Computing stoichiometric molecular composition from crystal structures, J. Appl. Crystallogr. 48 (2015) 85–91, https://doi.org/10.1107/S1600576714025904.

[43] A. Merkys, A. Vaitkus, J. Butkus, M. Okulič-Kazarinas, V. Kairys, S. Gražulis, COD::CIF::Parser: An error-correcting CIF parser for the Perl language, J. Appl. Crystallogr. 49 (2016) 292–301, https://doi.org/10.1107/S1600576715022396.

[43] M. Quirós, S. Gražulis, S. Girdzijauskaitė, A. Merkys, A. Vaitkus, Using SMILES strings for the description of chemical connectivity in the Crystallography Open Database, J. Cheminform. 10 (2018) 23, https://doi.org/10.1186/s13321-018-0279-6.

[44] M. Cantaluppi, N. Marinoni, F. Cella, A. Bravo, F. Cámara, G. Borghini, W. Kagan, An insight on the effect of sodium and silicon on microstructure and crystallography of high alumina cements, Cem. Concr. Res. 148 (2021) 106533, https://doi.org/10.1016/J.CEMCONRES.2021.106533.

[45] B.R. Currell, R. Grzeskowlak, H.G. Mldgley, J.R. Parsonage, the acceleration and retardation of set high alumina cement by additives, Cem. Concr. Res., 7 (1987) 420-432, https://doi.org/10.1016/0008-8846(87)90006-8.